Effects of layered crust on the coseismic slip inversion and related CFF variations: Hints from the 2012 Emilia Romagna earthquake

Massimo Nespoli[a], Maria E. Belardinelli[a], Letizia Anderlini[b], Maurizio Bonafede[a], Giuseppe Pezzo[c], Micol Todesco[d], Antonio P. Rinaldi[e]

[a] Department of Physics and Astronomy, University of Bologna, viale Berti Pichat 8, 40127 Bologna, Italy

[b] Istituto Nazionale di Geofisica e Vulcanologia, Centro Nazionale Terremoti, via Donato Creti 12, 40128 Bologna, Italy

[c] Istituto Nazionale di Geofisica e Vulcanologia, Centro Nazionale Terremoti, via di Vigna Murata 605, 00143 Roma, Italy

[d] Istituto Nazionale di Geofisica e Vulcanologia, Sezione di Bologna, via Donato Creti 12, 40128 Bologna, Italy

[e] Swiss Seismological Service, Swiss Federal Institute of Technology, ETHZ, Sonneggstrasse 5, 8055 Zürich, Switzerland

Abstract

The 2012 Emilia Romagna (Italy) seismic sequence has been extensively studied given the occurrence of two mainshocks, both temporally and spatially close to each other. The recent literature accounts for several fault models, obtained with different inversion methods and different datasets. Several authors investigated the possibility that the second event was triggered by the first mainshock with elusive results. In this work, we consider all the available InSAR and GPS datasets and two planar fault geometries, which are based on both seismological and geological constraints. We account for a layered, elastic half-space hosting the dislocation and compare the slip distribution resulting from the inversion and the related changes in Coulomb Failure Function (CFF) obtained with both a homogeneous and layered half-space. Finally, we focus on the interaction between the two main events, discriminating the contributions of coseismic and early postseismic slip of the mainshock on the generation of the second event and discuss the spatio-temporal distribution of the seismic sequence. When accounting for both InSAR and GPS geodetic data we are able to reproduce a detailed coseismic slip distribution for the two mainshocks that is in accordance with the overall aftershock seismicity distribution. Furthermore, we see that an elastic medium with depth dependent rigidity better accounts for the lack of the shallow seismicity, amplifying, with respect to the homogeneous case, the mechanical interaction of the two mainshocks.

Graphical abstract

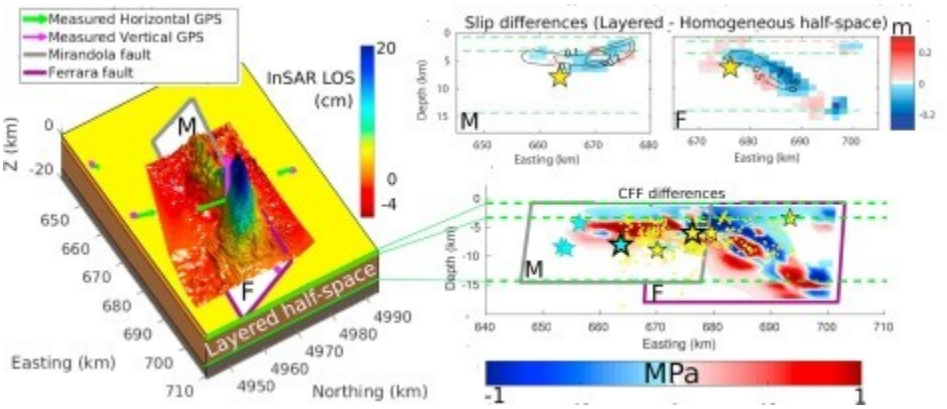

1. Introduction

In May 2012, a seismic sequence struck the Emilia Romagna region, in Northern Italy comprising 6 thrust events with $M_L \geq 5$ and two mainshocks with magnitude M_L5.9 and 5.8 (Fig. 1). The first mainshock (Mw 6.1 RCMT http://www.bo.ingv.it/RCMT) occurred on May 20th at 4:04 AM (local time) at a depth of 6.3 km, and was preceded by a M_L 4.1 event two hours before (01:13 AM, local time); the second main event (Mw 6.0 RCMT) occurred on May 29th at 9:00 AM (local time), at about 8 km of depth and 15 km southwest of the first mainshock (Scognamiglio et al., 2012). The entire seismic sequence was aligned along the E-W direction, and it extended for more than 50 km (e.g. Chiarabba et al., 2014, Govoni et al., 2014). The two main events caused 20 deaths, 350 injuries, the evacuation of about 15,000 people, and the collapse of several historical buildings, some of which of artistic interest. The seismic sequence had a great impact on the media and the population, also because it was accompanied by several surface effects, located in the near field, such as soil liquefaction (Lombardi and Bhattacharya, 2014), the increase of the water level in some wells (Marcaccio and Martinelli, 2012, Nespoli et al., 2016), and anomalous soil heating, associated with methane seepage (Capaccioni et al., 2015, Nespoli et al., 2015).

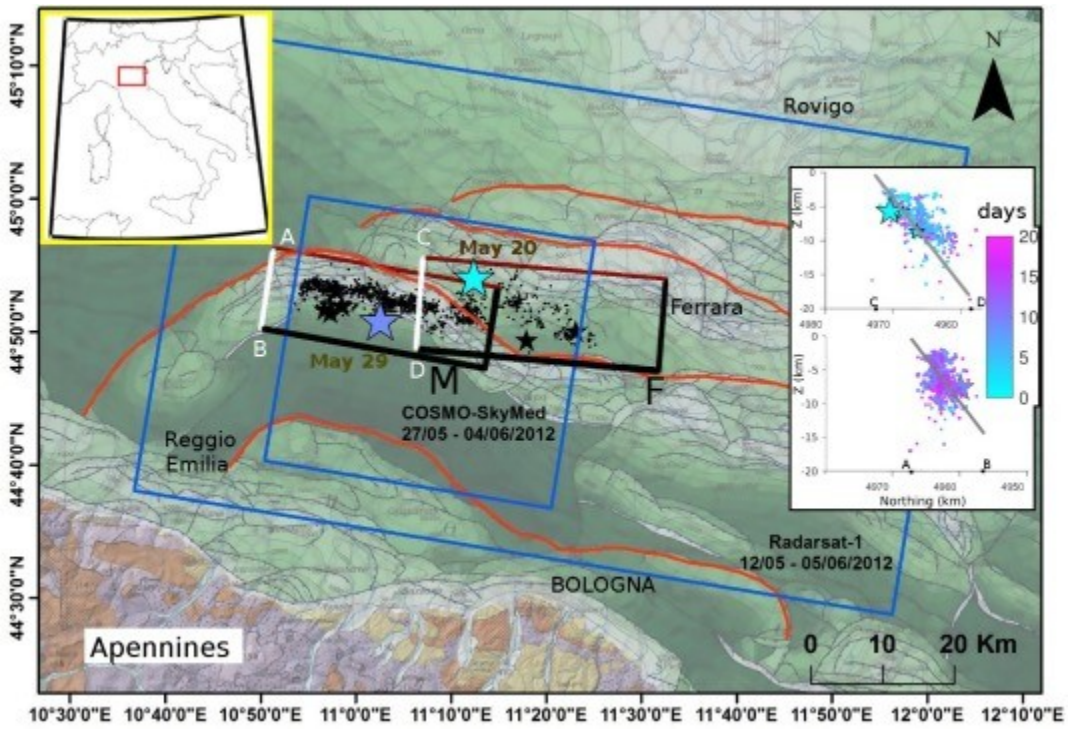

Fig. 1. Geostructural setting of area of the Emilia 2012 seismic sequence, showing the structural model of Italy and the vertically projected top traces of the main thrust fault planes (red lines). “M” indicates the Mirandola fault, “F” indicates the Ferrara fault. In green the isobaths lines of the Pliocene (modified after Bigi et al., 1983, Boccaletti et al., 2010, Picotti and Pazzaglia, 2008). Black dots represent the epicenters (stars Mw > 5.0) from Govoni et al. (2014). Blue rectangles are the footprints of the COSMO-SkyMed(CSK2) and Radarsat-1 satellite image pairs. Black boxes are the surface projections of modeled faults whose top edges are in dark red. White lines represent fault sections shown in the inset. (For interpretation of the references to colour in this figure legend, the reader is referred to the web version of this article.)

The epicenters were located in the Po River alluvial plain, where Plio-Quaternary sediments lie above the Apennines thrust belt system (Pezzo et al., 2013, Picotti and Pazzaglia, 2008, Toscani et al., 2009). These blind thrusts belong to the compressive mechanism induced by the slow northward movement of the Apennines chain with about 2 mm/yr of SW-NE shortening (Serpelloni et al., 2012, Devoti et al., 2011) and they are clearly outlined in seismic prospecting carried out by oil companies in the area (Boccaletti and Martelli, 2004, Regione Emilia-Romagna and ENI-AGIP, 1998). The historical seismicity of the region is well known and the two latest major events with magnitude above 4 date back to 1574 (M_L 4.63 ± 0.46) and 1570 (M_L5.44 ± 0.17) (Rovida et al., 2011).

The relocation of the 2012 seismicity distinctly highlights the activation of two fault zones: the Ferrara and the Mirandola faults (Govoni et al., 2014). The seismicity front migrated from east to west (Govoni et al., 2014): the events recorded between May 20th and May 29th are aligned along the Ferrara fault, with the exception of a western cluster spreading over the region where the two faults overlap (Fig. 1). After May 29th, the seismicity is mainly distributed close to the Mirandola fault plane. Interestingly, InSAR

data highlight a tail-shaped deformation pattern, that occurred spatially and temporally between the two mainshocks without relevant associated seismicity, interpreted as aseismic foreslip by Pezzo et al. (2013). An overview of focal mechanisms solutions proposed for the two mainshocks is reported by Cesca et al., 2013, Scognamiglio et al., 2016. The 2012 seismic sequence confirms the present activity of the external thrust belt, in agreement with the seismotectonic framework (Boccaletti et al., 2010).

Several fault models have been proposed for the two main events of the Emilia Romagna seismic sequence based on geodetic and/or seismological data collected during the activity period. Except for Volpe and Piersanti (2016), the inversions of the geodetic data were performed assuming dislocations embedded in a homogeneous elastic half-space (Serpelloni et al., 2012, Pezzo et al., 2013, Cheloni et al., 2016). It is worth to note that truly coseismic slip can be estimated inverting only GPS data, while InSAR data allow to estimate additional cumulative slip occurred within the time windows of interferograms. As in the present work we focus only on coseismic and early post-seismic phases, in Table 1 we report only the result performed by other authors by inverting InSAR data that cover the short time window around the two mainshocks. In all previous works, the hypocenter of the May 20th event was located on the Ferrara fault (F in Table 1), while the May 29th event was located on the Mirandola fault (M in Table 1). According to the model proposed by Pezzo et al. (2013), the slip of the May 20th event occurred along the Ferrara fault plane, even though some minor slip on the Mirandola fault is required to explain the tail-shaped deformation. Except for Serpelloni et al. (2012) who derived the fault geometry from non-linear inversions of GPS data, the other geometries were constrained by the seismicity distribution and by geological observations. Both Pezzo et al., 2013, Cheloni et al., 2016proposed a listric geometry for the two main fault planes (Table 1). Cheloni et al. (2016) also inverted the tail-shaped deformation pattern by assuming a third intermediate fault.

Table 1. Fault geometries for four different inversions for the May 20th (a) and May 29th (b) earthquakes. In the second column “F” stands for the Ferrara fault and “M” for the Mirandola fault.

	Active faults	**Dip (°)**	**Strike (°N)**	**Rake (°)**	**Max Slip (cm)**	**Top depth (km)**	**Number of patches**	**Data**
May 20 inversion								
Serpelloni et	F	37.7	109	86	99	4.9	1	GPS

	Active faults	Dip (°)	Strike (°N)	Rake (°)	Max Slip (cm)	Top depth (km)	Number of patches	Data
al. (2012)								
Pezzo et al. (2013)	F(2 seg.)	40 – 20	114	90	120	0.7 – 7.7	370	GPS, CSK1, RSAT 1-CSK2
	M(2 seg.)	45 – 30	95	85	30	0.7 – 9.6	275	
Cheloni et al. (2016)	F(2 seg.)	55 – 40	100	90	100	0–8	331	GPS
Present work	F	50	95	70	117 ± 2	0.7	345	GPS, CSK1, RSAT 1-CSK2
	M	50	100	90	35 ± 2	0.7	252	
May 29 inversion								
Serpelloni et al. (2012)	M	35.2	102	85.4	36	2.8	1	GPS
Pezzo et al. (2013)	M(2 seg.)	45 – 30	95	85	54	0.7 – 9.6	275	GPS, CSK2
Cheloni et al. (2016)	M(2 seg.)	65 – 30	100	90	60	0–8	331	GPS, CSK2

	Active faults	Dip (°)	Strike (°N)	Rake (°)	Max Slip (cm)	Top depth (km)	Number of patches	Data
Present work	M	50	100	90	70 ± 2	0.7	252	GPS, CSK2

The 2012 Emilia Romagna sequence is an interesting case history for the study of fault interaction, given the spatial and temporal proximity of the two mainshocks whose epicenters are separated by only 12 km distance. Many authors explored possible interaction between the corresponding faults based on the static Coulomb Failure Function changes (ΔCFF) analysis. Some authors found that the static CFF variations of the May 20th mainshock did not significantly contribute to bringing the fault of the May 29th mainshock closer to failure (Convertito et al., 2013, Cesca et al., 2013). Accounting for redistribution of coseismic pore pressure changes leads to equivalent conclusions (Volpe and Piersanti, 2016), although based on simplified assumptions. On the contrary, Ganas et al. (2012) indicated that the second mainshock was likely triggered by the first one, as its hypocenter is located in a positive CFF zone according to their fault model. Performing the ΔCFF analysis in a homogeneous half-space, both Cheloni et al., 2016, Pezzo et al., 2013 suggested that the second mainshock was triggered by the presumably aseismic slip that explains the aforementioned tail-shaped deformation. The contrasting conclusions, obtained with different source models, emphasize that the stress transfer problem is extremely sensitive to both the fault geometry and the elastic structure of the medium.

In this work we estimate the slip distributions occurred during the two time intervals from May 12 to May 27, 2012 (T1) and from May 27 to June 4, 2012 (T2), performing a linear joint inversion of the geodetic data from both GPS receivers and InSAR satellites (same data sets as Pezzo et al. 2013). With respect to previous studies (Table 1) we use a simpler fault geometry (no third fault and uniform dip angles) constrained on the basis of the distribution of relocated seismicity (Fig. 1) with location errors smaller than 1 km (Govoni et al. 2014). This choice relies on the preferability of the simplest geometrical model (consistent with seismic and geological evidences), that explains all the data with the same accuracy as previous studies.

This work especially focuses on:

1. understanding the effects of a more realistic layered medium on the inversion results, highlighting the differences between the slip distributions obtained with homogeneous or layered half-space;

2. assessing the effects of the rake angle assumed in the data inversion process;

3. investigating if a third fault plane is required by the data here inverted;

4. comparing the ΔCFF calculated when both faults causing the mainshocks are embedded in a homogeneous or in a layered half-space;

5. comparing the spatial distribution of the seismicity occurred in the first 30 days of the sequence with the resulting slip distribution and related ΔCFF.

2. Geodetic data

The dataset includes the displacements measured by 18 GPS stations (Serpelloni et al., 2012, Table S1) and the available SAR interferograms spanning three different time windows: from May 12th to June 5th for RADARSAT-1, from May 19th to May 23th for COSMO Sky-Med (hereinafter CSK1) and from May 27th to June 4th for the second COSMO Sky-Med interferogram (hereinafter CSK2). For the May 20th event, only three GPS stations, located within 30 km from the epicenter, recorded a coseismic displacement in the order of centimeters (Fig. 2a and b): SGIP, SERM and MO05. On May 29th, all available GPS stations were located in the far field and recorded low displacements (Fig. 2c).

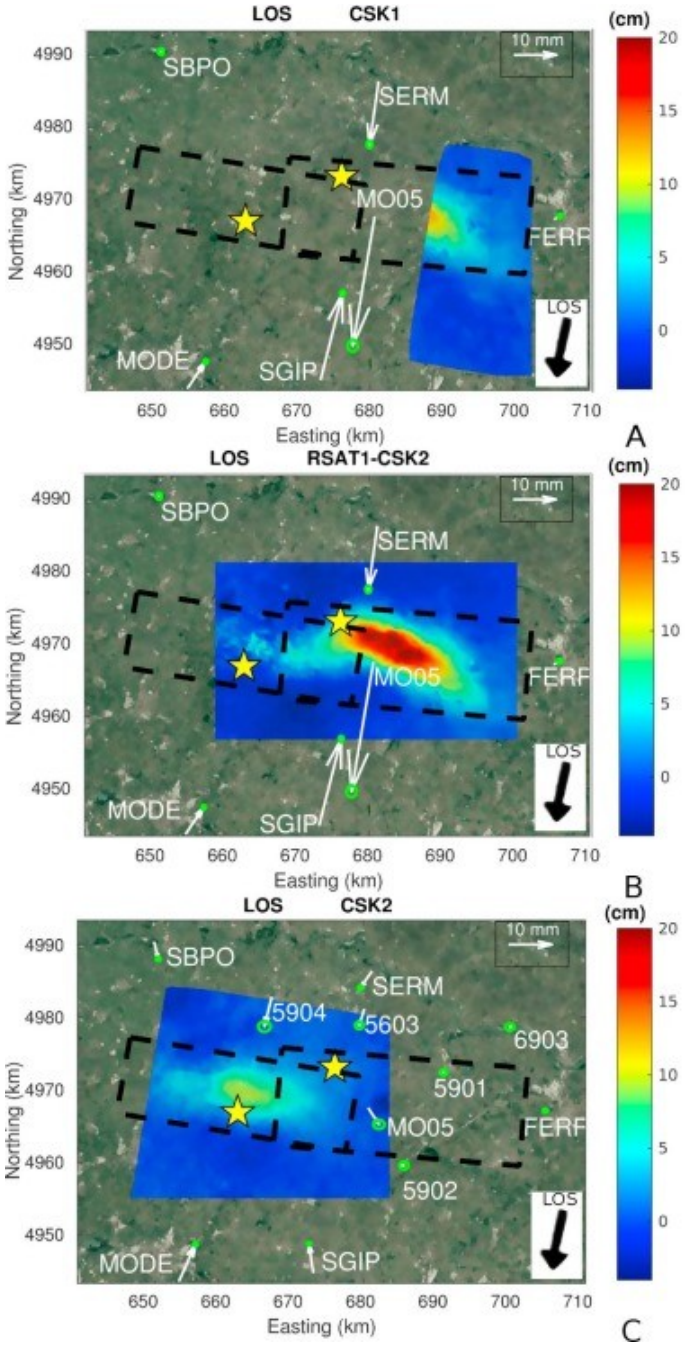

Fig. 2. InSAR LOS displacements of the May 20, 2012 earthquake measured by CSK1 (a), RSAT1-CSK2 (b) and of the May 29 earthquake measured by CSK2 (c). White arrows represent coseismic horizontal displacements measured in GPSstations with related uncertainties (green ellipses). Stars represent the May 20th (easternmost) and the May 29th (westernmost) epicenters.

Concerning InSAR data, the CSK1 and CSK2 interferograms (Fig. 2a and c) are two about 40 × 40 km images obtained from descending satellite orbits. As shown in Fig. 3 (black boxes), the 4-days time span of the CSK1 images could be used to infer the easternmost part of the displacement field due to the 20th of May seismic event, while the 8-days interval of the CSK2

interferogram mostly relates to the displacement of the 29th of May earthquake.

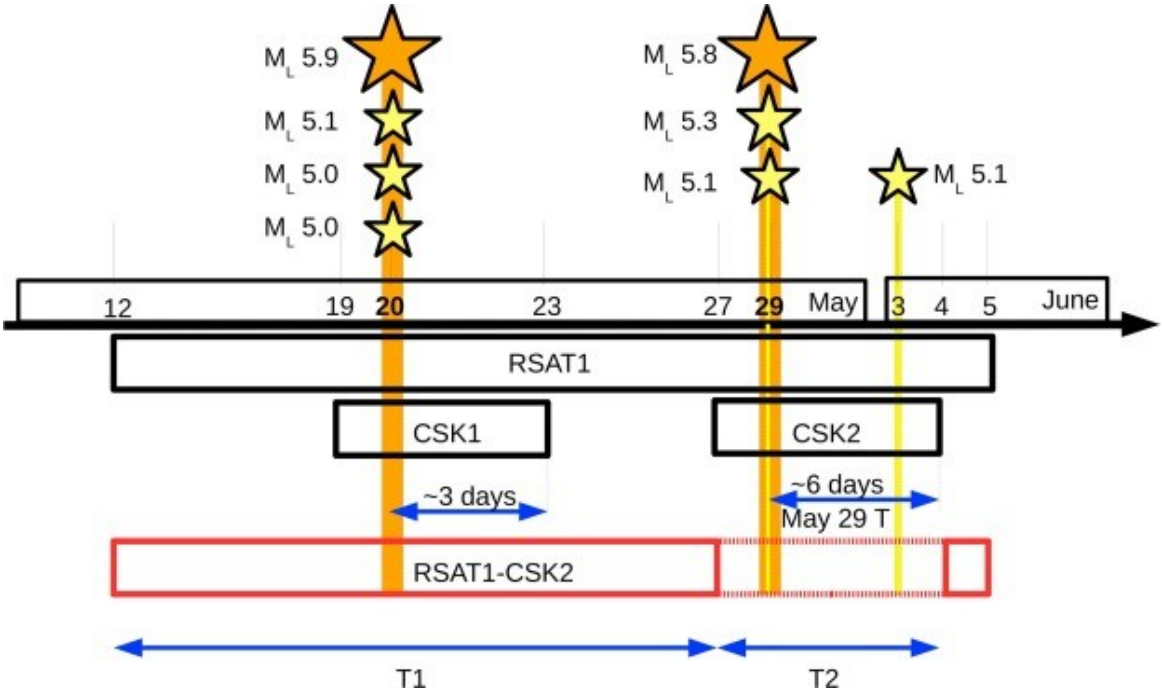

Fig. 3. Graphical illustration of time windows covered by InSAR image pairs (black boxes for RSAT1, CSK1 and CSK2, red boxes for RSAT1-CSK1). The stars represent the major events ($M_L \geq 5$) of the seismic sequence. The geodetic data inversion is performed to obtain cumulative slip occurred in the two periods T1 and T2.

A wider and whole representation of the displacement field for the May 20th earthquake is given by the RSAT1-CSK2 map (Fig. 2b) obtained by subtracting the CSK2 unwrapping interferogram from the RSAT1 image (Pezzo et al., 2013, Volpe and Piersanti, 2016). The RSAT1 interferogram has been obtained by a 100×100 km image pair referred to a wide time window (Fig. 3) that includes the effects of the two mainshocks as well as the post-seismic deformations and the effects of all the seismicity that occurred in the lag time between the two main events. The RSAT1-CSK2 covers an area of about 65×110 km and two time windows: from May 12th to 27th and from June 4th to 5th (red boxes in Fig. 3). On the basis of the DInSAR CSK time-series of selected points in the area of maximum deformation (Fig. S2 in Cheloni et al., 2016), during the second time-window (4–5 June) less than 3 mm of postseismic deformation can be estimated, hence its contribution can be neglected in the RSAT1-CSK2 map. Accordingly, this dataset is suitable to represent the coseismic and early post-seismic deformation caused by the May 20th mainshock. The RSAT1-CSK2 map has a positive Line of Sight (LOS) displacement distributed over an approximately elliptical area where a maximum value of about 21 cm is obtained (Fig. 2b). West of the May 20th epicenter, the positive displacement extends towards the May 29th epicenter with a tail-shaped pattern and a maximum value of about 7 cm. In the CSK2 map (Fig. 2c), the pattern of LOS displacements of

the May 29th event shows an EW-oriented elliptical shape, with a maximum positive displacement of about 10 cm. The deformation occurring between the two epicenters was not associated with
significant foreshocks or aftershocks. One hypothesis suggests that it occurred as coseismic slip of the May 20th event, while another possibility includes aseismic slip occurring after the first mainshock along a different fault plane, namely the May 29th fault plane (e.g. Pezzo et al., 2013, Volpe and Piersanti, 2016) or a third one (Cheloni et al., 2016).

While in Cheloni et al. (2016) post-seismic deformation was also considered, we rather want to focus on the May 20–May 29 period using the spatially densest data-set, which covers relatively narrow time windows (T1 and T2) around the two mainshocks.

3. Data modeling

The InSAR CSK1 and RSAT1-CSK2 displacements (Fig. 2a and b) have been inverted jointly with the available GPS co-seismic data (Table S1) for the May 20th mainshock to estimate the co-seismic and early post-seismic slip distribution on the Ferrara and Mirandola faults. Similarly, we jointly inverted InSAR (CSK2, Fig. 2c) and GPS displacements (Table S1) of the May 29th event in order to recover the slip distribution on Mirandola fault plane, analyzing their potential interaction. Fault planes of the Ferrara and Mirandola thrusts (whose geometry parameters are reported in Table 1) are subdivided into square patches of 1.5 km length resulting into 23×15 patches for the Ferrara fault and 21×13 patches for the Mirandola one.

The slip inversions have been performed considering the fault planes embedded both in a homogeneous elastic half-space (HOM case), and in a layered elastic half-space (LAY case). For the homogeneous model, we assume a Poisson's ratio $\nu = 0.25$ and a rigidity $\mu = 30$ GPa, that are common values in inversions performed in homogeneous half-spaces (e.g. Pezzo et al., 2013, Cheloni et al., 2016). The elastic parameters of the layered model were taken from CRUST1.0 (Laske et al., 2013) with WGS84: 44.8 N, 11.3 E as a query point located in the center of the investigated domain. The rigidity and the Poisson's module, desumed from Vs, Vp and density profiles, along depth are plotted in Fig. 4. All the available crustal models for the investigated region (e.g. Laske et al., 2013, Govoni et al., 2014, Molinari et al., 2015) present a strong discontinuity at about 3.5 km depth. In particular, CRUST1.0 and a 3D crustal model, MAMBO (Molinari et al., 2015), are in good agreement if compared in the same query point (Fig. 4 and Fig. S1, Supplementary material). In the discussion section, we will see that we obtain negligible (i.e. within the estimated uncertainties) differences in the slip distribution if the inversion is performed in the three different layered 1D crustal models available for the investigated region, i.e. CRUST1.0, MAMBO (Fig. S1) and Fig. 4 in Govoni et al. (2014). We compute the final slip distribution estimating the best slip solution that minimizes the discrepancy between observed data and expected displacement pattern. In the following

paragraph the methods and techniques used to perform the inversions in the HOM and LAY cases are reported in details.

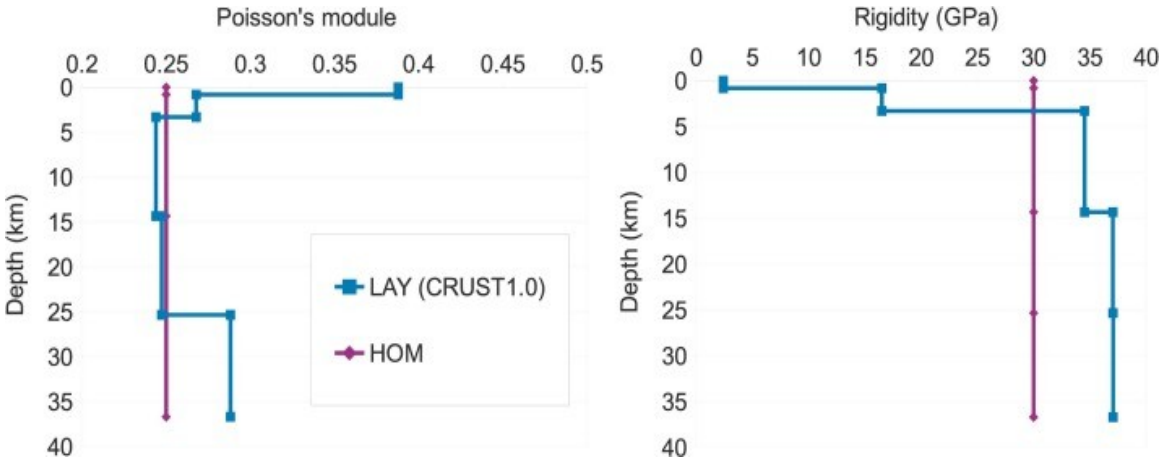

Fig. 4. One-dimensional crustal model used in the LAY and HOM case: rigidity (GPa) and Poisson's module as functions of depth are represented with solid lines (from CRUST1.0, Laske, 2013). For the HOM case a Poisson modulus $\nu = 0.25$ and a rigidity modulus of 30 GPa are assumed.

3.1. Inversion method

The main equation representing the linear relation between model parameters and ground deformations is:

$$\mathbf{d} = \mathbf{G}\mathbf{s} \quad \text{i.e.} \quad \begin{bmatrix} \mathbf{d}_{\mathbf{GPS}} \\ \mathbf{d}_{\mathbf{SAR}} \end{bmatrix} = \begin{bmatrix} \mathbf{G}_{\mathbf{D}} & \mathbf{G}_{\mathbf{R}} \end{bmatrix} \begin{bmatrix} \mathbf{S}_{\mathbf{D}} \\ \mathbf{S}_{\mathbf{R}} \end{bmatrix} \tag{1}$$

where **s** is the vector of the model parameters to be estimated by inversion, i.e. slip on individual fault patches, $\boldsymbol{s}_D$, and the three ramp terms, $\boldsymbol{s}_R$, correcting possible satellite orbital error. In Eq. (1), **d** is the displacement data vector (GPS + InSAR), and **G** is a linear operator connecting model and data vectors by means of two elements: $\mathbf{G_D}$ is a matrix of Green's functions relating the model parameters $\boldsymbol{s}_D$ to the surface displacements, and $\mathbf{G_R}$ is the planar ramp matrix for InSAR data needing a correction (Zebker et al., 1994). Given that the Green's functions strictly depend on the specific crust representation, for the HOM case we used Okada's formulation (Okada, 1992), whereas for the LAY case, each $\mathbf{G_D}$ element was evaluated through the EDGRN-EDCMP code (Wang et al., 2003), which allows us to compute surface and subsurface displacements, strain, and stresses in a layered elastic half-space, due to rectangular dislocations. In order to form the kernel $\mathbf{G_D}$, we compute the displacement due to a uniform unit slip on each fault patch at the observation point locations (GPS stations and InSAR points), following the method by Hearn and Burgmann (2005). With the aim of studying the influence of the elastic parameters on the inversions, we also compute two additional G kernels assuming the same crustal model of the

LAY case, but considering respectively a 20% increase of the Poisson module and 20% decrease of rigidity in the shallowest 3.3 km of depth, with respect to the LAY case. We found that the effects on the G kernel of the rigidity lowering and of the Poisson number increasing are opposite but of comparable intensity (Fig. S1d and e). We must consider that in the LAY case, the rigidity contrast in the shallowest layers is up to 90%, while the Poisson number contrast is up to 50%. This makes likely that the rigidity decrease in the shallowest layer is the major reason of the G kernel difference between the LAY case and the HOM one (Fig. S1f).

In order to smooth the slip distribution, we also apply a regularization constraint (∇2SD=0), where the Laplacian operator is expressed with the finite differences approximation of the second derivative, as proposed by Harris and Segall (1987). Then, we can express Eq. (1) as:

$$\begin{bmatrix} \mathbf{Wd} \\ \mathbf{0} \end{bmatrix} = \begin{bmatrix} \mathbf{WG} \\ \beta\nabla^2 \end{bmatrix}$$

(2)

where β is the smoothing factor that has been estimated using a trade-off curve between the data misfit and the slip distribution roughness ∇2SD=0, while W represents the relative weight between GPS and InSAR datasets. Following the method by Belardinelli et al. (2003), the weight matrix W was defined by using the F to N ratio, where F represents the degrees of freedom (DoF) of each dataset and N is the number of data ($N_{GPS} = 13 \times 3$, $N_{SAR} = 6914$ for the May 20th; $N_{GPS} = 18 \times 3$, $N_{SAR} = 4413$ for the May 29th). For GPS data, we accounted for one DoF ($F_{GPS} = 1$), while for the InSAR measures we considered as DoF the number of fringes (Pizzi and Scisciani, 2012) plus one further DoF given by the absolute position of the interferograms ($F_{SAR} = 8$ and $F_{SAR} = 6$ for the events on May 20th and 29th, respectively). In Fig. S2, for both T1 and T2 inversions, we report the tradeoff curves whose knee point identifies the β value we selected for the smoothing factor (e.g. Arnadottir and Segall, 1994, Bürgmann et al., 2005, Amoruso and Crescentini, 2008).

Moreover, in order to obtain that the whole rupture area reasonably tapers to zero at its borders (Pedersen et al., 2003), no-slip bounds have been applied at fault edges. We compute the final slip distribution estimating the best model parameter set (**s**) that minimizes the discrepancy between the observed data and the expected displacement pattern. The minimization is achieved by using a constrained linear least squares inversion scheme (Coleman and Li, 1996). The misfit function to be minimized is the Weighted Residual Sum of Squares (WRSS):

$$WRSS = (\mathbf{d}^{\mathrm{mod}} - \mathbf{d}^{\mathrm{obs}})\mathbf{W}(\mathbf{d}^{\mathrm{mod}} - \mathbf{d}^{\mathrm{obs}}) \quad (3)$$

The rake angle (θ) is kept fixed for all the patches belonging to the same fault surface (Table 1). Indeed, to choose the best value for the Ferrara fault, we performed several inversions for the May 20 event, varying the rake angle in the range $45° < \theta < 135°$ (as indicative for a mostly inverse-slip fault solution). The WRSS analysis for both HOM and LAY cases clearly indicates that rake angles greater than 90° are very unlikely for all datasets (Fig. 5). Lower rake values significantly decrease the WRSS, which reaches a flat minimum between 60° and 70°, as suggested by both GPS and RSAT1-CSK2 datasets. The minimum is not clear for the CSK1 dataset, whose recorded area does not include the region of maximum LOS displacement (Fig. 2a). Due to the small difference in WRSS values for rake angles below 80° for the Ferrara fault (Fig. 5), we do not consider appropriate assuming the rake angle as variable along the fault surfaces during the inversion process. Our results suggest that the Ferrara fault had a non-negligible eastward slip component during the main event of May 20 and it was much closer to a transpressive rupture rather than to a pure inverse-slip fault. In the following of this paper we will use the rake value of 70° close to the average focal mechanism.

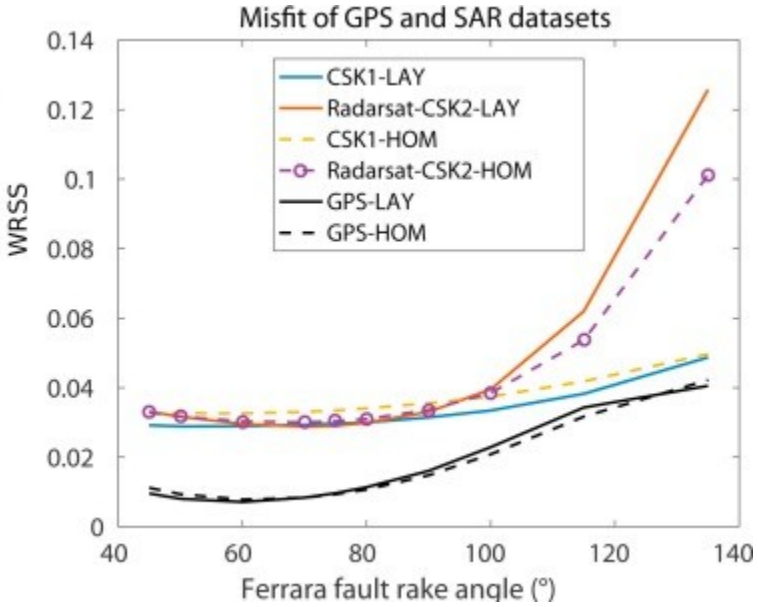

Fig. 5. Model WRSS with respect to InSAR and GPS data as a function of the rake angle of the Ferrara fault, for both HOM (dashed lines) and LAY (continuous line) cases.

The resolution analysis of the estimated slip distributions for both faults in T1 and T2 periods is performed calculating the Resolution Length (RL) proposed by Ader et al. (2012). RL represents the characteristic size of the smallest inhomogeneity of slip that can be detected by data. Therefore, to consider as resolved a spatial feature of slip, the RL should be constant on it

and smaller than the feature size itself (Anderlini et al., 2016). Figs. S3 and S4 show the obtained RL values, that are smaller than 2 km in most of the fault surfaces above 8 km of depth, thanks to the high-density InSAR data distribution, inferring that most of the spatial features of slip distributions are well resolved.

The error on the slip distribution is evaluated following the approach used by Biggs et al. (2006): errors for slip on individual patches are determined using a Monte-Carlo simulation technique. We performed 100 minimum-misfit solutions obtained with randomly perturbed LOS displacements of InSAR interferograms. The applied perturbations are normally distributed with a standard deviation of 1 cm, as the observational error (i.e. 2σ) of the InSAR interferograms here used is ±2 cm. The standard deviation of the 100 resulting slip values on each patch estimates the error (or better, confidence interval amplitude) on the slip in that patch. The resulting distributions of slip errors are shown in Figs. S5 and S6 for T1 and T2.

4. Slip distributions of May 20th and 29th events

Fig. 6a and b show the slip distributions resulting from data inversion during the period T1 on the Ferrara and Mirandola fault planes for the HOM and the LAY case, respectively. In both cases, similar slip patterns are obtained with a maximum slip area located near the center of the Ferrara fault plane between 7 km and 10 km depth. The maximum absolute slip is 1.28 ± 0.02 m for the HOM case, and 1.17 ± 0.02 m for the LAY case. Slip values larger than 0.5 m already exist below 2 km of depth. In both cases, a less resolved relative maximum of slip is located at a depth of about 13 km, with amplitude 0.37 ± 0.04 m and 0.38 ± 0.04 m for the HOM and the LAY cases, respectively. On the Mirandola fault plane, slip is distributed along a shallow tail-shaped pattern reaching a maximum of 0.35 ± 0.01 m and 0.35 ± 0.02 m for the HOM and LAY cases, respectively. The slip on the Mirandola fault plane results from the inversion of the tail-shaped deformation pattern in the RSAT1-CSK2 dataset (Fig. 2b).

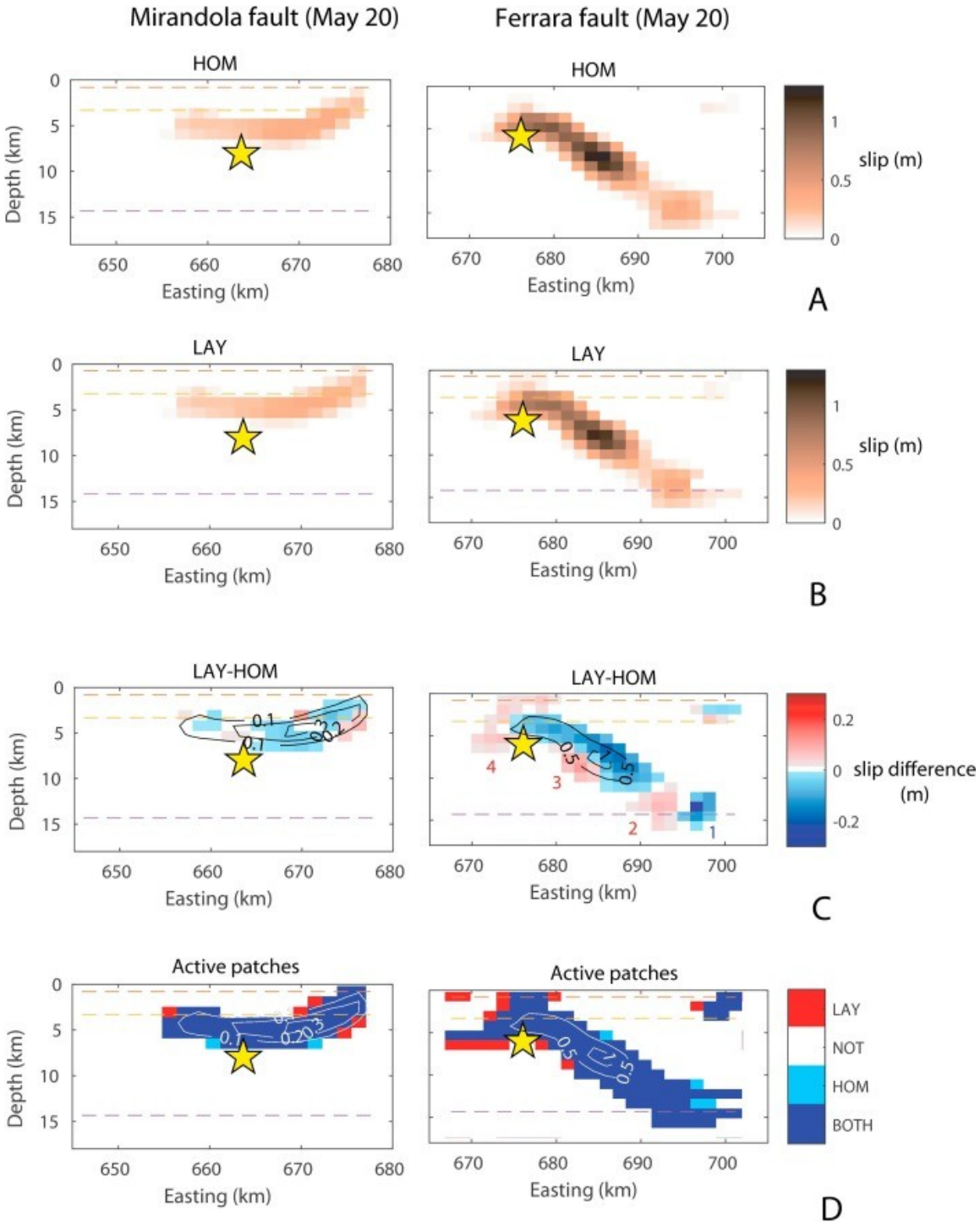

Fig. 6. Results for the slip distribution in the HOM (a) and LAY (b) case on the Ferrara (right) and Mirandola (left) faults, as obtained from available data covering the T1 period (May 20 mainshock). Panel (c) shows slip differences between the LAY and the HOM case. Active patches (slip values larger than 0) are shown in panel d: dark blue represents active patches in both cases, light blue and red represent the patches which are active only in the HOM and LAY case, respectively. The stars represent the May 20 hypocenter (on the Ferrara fault) and the May 29 hypocenter (on the Mirandola fault). Slip values on the Ferrara (Mirandola) fault larger than 0.5 m (0.1 m) are contoured in black (c), and in white (d) as obtained in the LAY case. The dashed lines represent the CRUST1.0 elastic discontinuities (see Fig. 4).

Fig. 6c shows the differences between the slip values obtained for the HOM case with respect to the LAY case (LAY-HOM) on both fault planes. The slip distribution for the LAY case (black contour) is also shown for comparison. For both faults, the HOM case generally produces 0.1–0.2 m larger slip throughout the maximum slip area (blue areas). However, just below the maximum slip region on the Ferrara fault (label #2 and 3, in Fig. 6c, and at shallower depths #4), the inverted slip is larger for the LAY case (red areas). In the shallow zone #4, this can be related to the lower rigidity assigned in the LAY case above −3.3 km of depth compared to the HOM case: indeed, a larger slip is required in this region to reproduce the observed ground surface deformation. Fig. 6d shows the location of non-vanishing slip patches: in the LAY case, the rupture occurs at several additional patches with respect to the HOM case, in particular at the shallowest and most western portion of the Ferrara fault, above 10 km of depth. Finally, Fig. 7 shows the observed GPS and InSAR ground surface displacements (panels a and d), as well as the modeled displacement obtained in the LAY case (panels b and e). The LOS displacements residuals are generally in the range −2 to +2 cm (Fig. S7), except for some scattered points with residuals up to 6 cm (Fig. 7c).

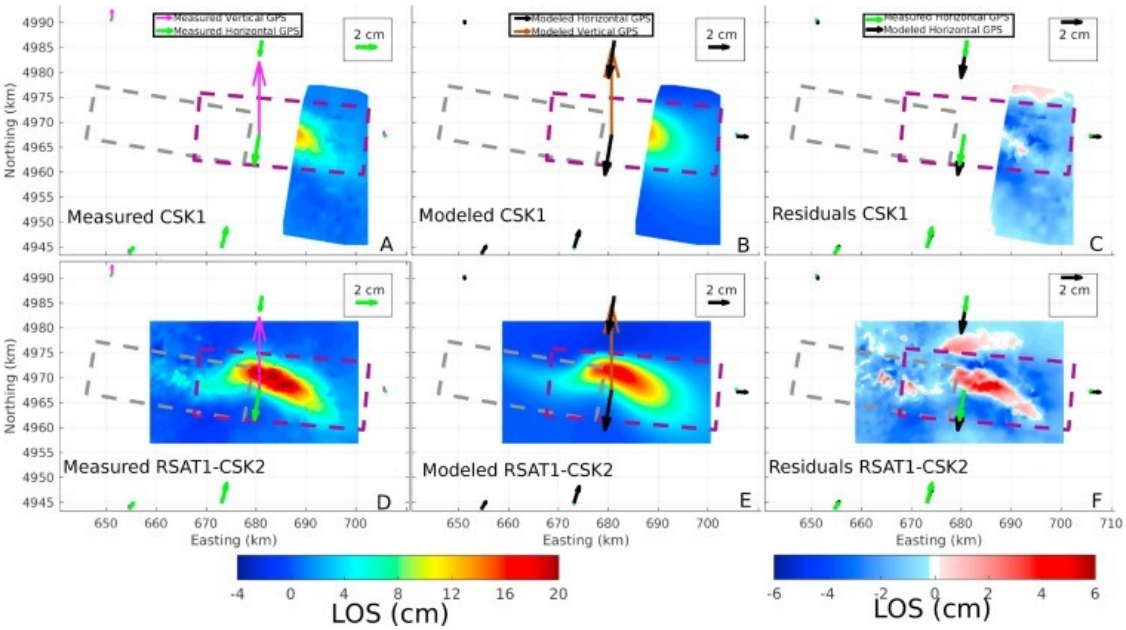

Fig. 7. Measured (a), modeled (b) and residuals (c) of CSK1 LOS displacements. Measured (d), modeled (e) and residuals (f) of RSAT1-CSK2 LOS displacements. Modeled results are obtained in the LAY case. Green and black arrows are respectively the measured and modeled horizontal GPS displacements, the magenta (a, d) and brown (b, e) arrows are the measured and modeled vertical GPS displacements, respectively.

Fig. 8a shows the resulting slip distribution after data inversion during the period T2 on the Mirandola fault for both HOM and LAY cases. In the HOM case the maximum slip (0.80 ± 0.02 m) is greater than in the LAY case (0.70 ± 0.02 m), similarly to the period T1. Interestingly the maximum slip is located in different positions: for the HOM case it is found about 5 km more

eastward than for the LAY case. Accordingly, slip differences (Fig. 8b) are large (up to 0.5 m). In both cases, the rupture mainly grows below 3.3 km depth where the rigidity is higher in the LAY case. This allows the inverted slip to be deeper for the LAY case. The rupture area extends more along the strike direction at intermediate depths for the HOM case (3.3–8 km, Fig. 8c). It is worth noting that the May 29th hypocenter is within the estimated rupture area only for the LAY case and it is located at the edge of the high-slip region. Accordingly, for the T2 period a more western and deeper rupture is obtained in the LAY case than the HOM case (Fig. 8b). Similar differences of slip distributions can be inferred comparing the one obtained by Volpe and Piersanti (2016)in a heterogeneous medium, with the one computed by Pezzo et al. (2013) in a homogeneous half-space. Such differences can be interpreted as likely due to the different structural model assumed by Volpe and Piersanti (2016). In our study the discontinuity at 3.3 km of depth is responsible for the major differences between the inversion results obtained in the HOM and LAY cases. Our findings should be taken into account in the analysis of seismic sequences where in particular a high contrast in the velocity structureoccurs at shallow (~few km) depth.

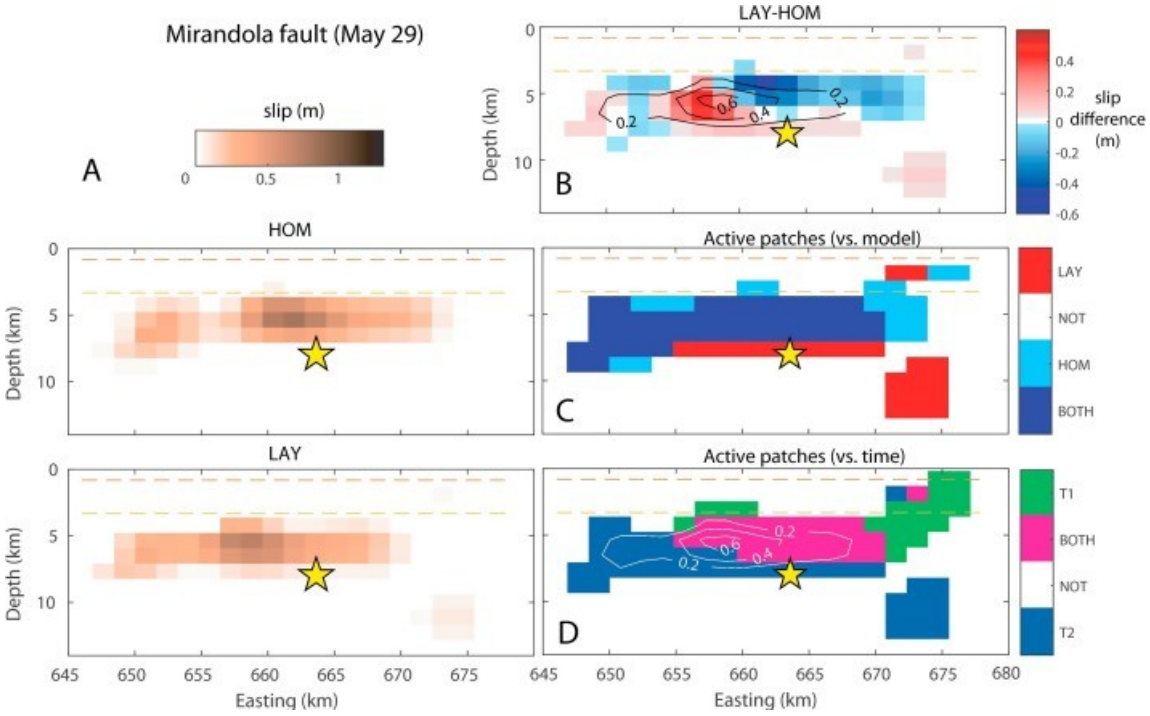

Fig. 8. (a) Results for the slip distribution in the HOM and LAY case on the Mirandola fault, as obtained from available data covering the T2 period (May 29 mainshock). Panel (b) shows slip differences between the LAY and the HOM case. Active patches (slip values larger than 0) are shown in panel (c): dark blue represents active patches in both cases, light blue and red represent the patches which are active only in the HOM and LAY case, respectively. Panel (d) shows active patches during the T1 period only (green), the T2 period only (blue) and during all the investigated time interval (magenta). The stars represent the May 29 hypocenter. Slip values larger than 0.2 m are contoured in black (b), and in white (d), as obtained in the LAY case. The dashed lines represent the CRUST1.0 elastic discontinuities (see Fig. 4).

Fig. 8d shows the location of active patches of the Mirandola fault during either T1 (green patches) or T2 (blue patches) or both time intervals (magenta patches) for the LAY case. A shallow and eastern area of the Mirandola fault was activated only during period T1. However, during T2 western and deeper portions of the fault were newly activated, besides its middle part. It can be then inferred a likely westward slip propagation from T1 to T2. Our model reproduces both the InSAR and GPS displacement due to the May 29th event (Fig. 9) with residuals smaller than 4 cm (Fig. 9c and S8). The average RMS (Root Mean Squares) for both T1 and T2 periods and for each dataset are generally slightly lower for the LAY case with respect to the HOM case (Table S2) and histograms of residuals are in Figs. S7 and S8. The horizontal GPS vectors show a general deformation pattern that converges towards the area with the greatest uplift, which is well captured by our model (Fig. 9). The errors on the slip distributions for both periods T1 and T2 show that the inversion leads to a precise estimation of the slip values, particularly above 10 km of depth (Figs. S5 and S6), where also the resolution length is finer (Figs. S3 and S4): 85% of non-vanishing slip patches is above the 2σ threshold (93% above σ). From the errors estimation we can also infer that the slip differences between the LAY and the HOM model are meaningful, as 50% of slip patches has differences greater than 2σ (1σ, 70%).

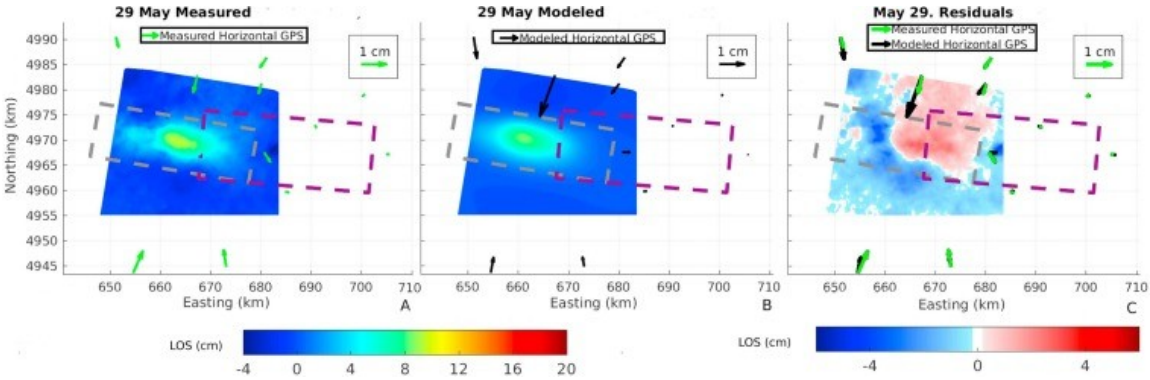

Fig. 9. Measured (a) and modeled (b) LOS cumulative displacement occurred in the T2 period. Measured LOS displacements (a) are from the CSK2 interferogram. Modeled LOS displacements (b) are obtained in the LAY case. Green (a, c) and black (b, c) arrows are the measured and modeled horizontal GPS displacements, respectively. (c) Residuals distribution.

Finally, we explore the effect of inverting the geodetic datain the period T1 using a third additional fault with the same geometry of the Mirandola fault but translated 4 km eastward, which is located between the two main faults (Fig. S9). As we can see from Fig. S10 the 3-faults inversion yields some localized slip on the third fault plane. Due to the larger number of patches, *k*, this inversion leads to a slightly lower total misfit, $M = \sum_{i=1}^{N} |(d^{obs}(i) - d^{mod}(i))/W_i|$, where w_i is the weight of the observation point *i*. In order to discriminate if increasing the number of faults really

improves the model or not, we applied the corrected Akaike's Information Criterion (*AICc*) test (Hurvich and Tsai, 1989, Amoruso and Crescentini, 2008). The *AICc* test states that the solution with the smallest AICc value is most likely to be correct, where AICc is defined as

$$AICc = \frac{2\,NK}{N-K-1} + NIn\,\frac{M}{N} \quad (4)$$

In Eq. (4), $N = 6953$ is the number of data, M is the non-normalized misfit, k is the number of parameters (patches) and for the 2-faults LAY model we have $M = 77.6$, $k = 597$, while for the 3-faults LAY model we have $M = 74.8$, $k = 849$. Applying this test, we found that the AICc value of the 3-faults model (−29651) is larger than that of the 2-faults model (−29947). For the 2-fault model, it is worth noting that in the HOM case the misfit M is larger (M = 81.9, AICc = −29575) compared to the LAY case.

The slip distribution estimated during T2 has an equivalent seismic moment of 9.8×10^{17} Nm corresponding to Mw = 6.0 in agreement with the RCMT catalog. In the case of T1 we estimate an equivalent seismic moment of 2.3×10^{18} Nm corresponding to Mw = 6.2. The difference with respect to the RCMT estimate (Mw = 6.1) is probably due to the contributions of both early postseismic deformation and the three largest seismic events ($M_L \geq 5$) occurred in T1 (see section Geodetic data and Fig. 1, Fig. 3). It is worth noting that the seismic moment equivalent to the slip distribution on the Ferrara fault is 1.8×10^{18} Nm, a value close to the seismic moment corresponding to Mw = 6.1 estimated by RCMT (1.6×10^{18} Nm). Accordingly, during the T1 period, it is likely that slip on the Ferrara fault was mostly coseismic, while the slip distribution on the Mirandola fault might have been aseismic, possibly postseismic.

5. The CFF changes

In this section, we evaluate changes in the Coulomb Failure Function, ΔCFF, during the May 20–29 sequence in both the LAY and the HOM cases. The ΔCFF is defined in the following equation, compatible with the convention of positive stress for extension:

$$\Delta CFF = \Delta\tau + \mu(\Delta\sigma_n) \quad (5)$$

where $\Delta\tau$ and $\Delta\sigma_n$ are the shear and normal stress changes calculated for a specific receiver fault geometry, and μ′ is the effective frictional coefficient ($\mu' = \mu(1 - B) = 0.4$, $\mu = 0.8$, $B = 0.5$ according to Harris (1998) and references therein, with μ frictional coefficient and B the Skempton's coefficient).

In Fig. 10, positive ΔCFF values delimit areas where activation of receiver faults oriented as the Mirandola fault are potentially favored by the occurrence of the May 20th mainshock, while negative values indicate areas where the activation is hindered. Generally it is worth recalling that a positive ΔCFF is not a sufficient condition to induce failure on a receiver fault,

as confirmed by studies correlating ΔCFF and aftershock distributions (e.g. Hardebeck et al., 1998). In the HOM case (Fig. 10a cross section), the shallowest negative lobes are wider than in the LAY case (Fig. 10b cross section), where above the discontinuity at 3.3 km of depth, a lower rigidity is assumed. Below this depth, positive lobes are 10 km wider for the LAY case, due to the greater rigidity values. The hypocenter of the May 29th event falls within one of the positive lobes in both cases: for the LAY case, we estimate $\Delta CFF = 0.35$ MPa, while for the HOM case $\Delta CFF = 0.32$ MPa. This indicates that the May 29th earthquake was likely favored by the previous rupture. The differences of $|\Delta CFF|$ values between the LAY and HOM case are emphasized in Fig. 10c which shows that the HOM case overestimates the CFF variations mainly above 3.3 km of depth, while below, except few small regions, the LAY case produces greater CFF changes. The largest ΔCFF differences in absolute value occur near the rupture plane, ranging between ± 2 MPa. Fig. 10d shows the ΔCFF without considering the contribution from slip occurred on the Mirandola fault during T1 (i.e. only slip on the Ferrara fault is considered). From the N-S section we can see that positive and negative lobes are drastically reduced in amplitude. Observing the horizontal section in the easternmost part, where the Ferrara fault slip had the greatest influence, the ΔCFF distribution results almost the same as in Fig. 10b, while ΔCFF is lower in the western part. In particular, at the location of the May 29th hypocenter the ΔCFF value decreases down to only 2×10^{-3} MPa which is still considered capable to promote aftershocks (Kilb et al., 2002, Rajput et al., 2005).

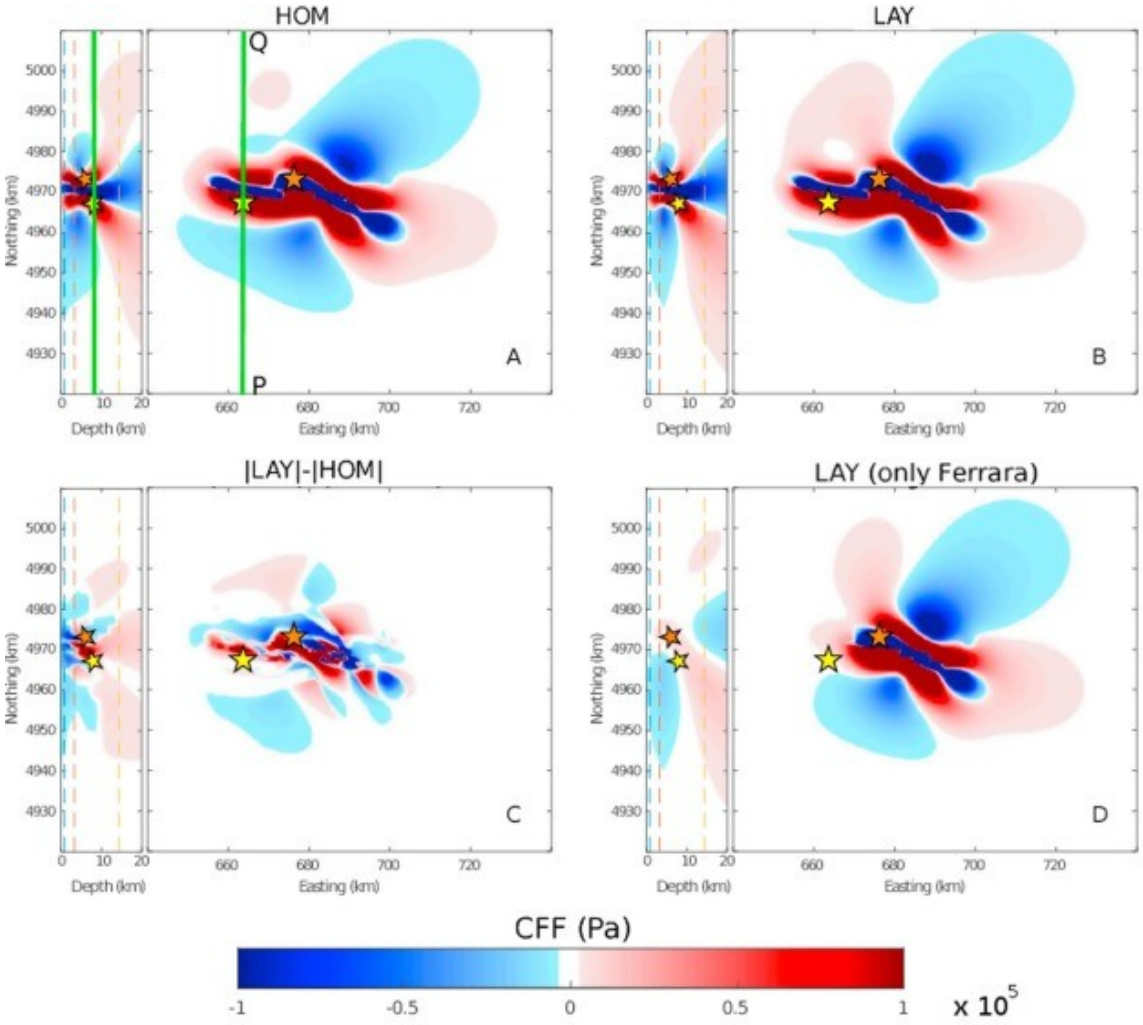

Fig. 10. Spatial distribution of the CFF changes caused by slip on the Ferrara and Mirandola faults for the HOM case (a) and LAY case (b), as obtained from the inversion of available data in the T1 period (Fig. 6a). (c) Distribution of the difference between the absolute value of ΔCFF in the LAY case with respect to the HOM case. Negative values indicate that the |ΔCFF| of the LAY case is lower than the one of the HOM case. (d) ΔCFF distribution is obtained for the LAY case without considering the slip occurred on the Mirandola fault in the T1 period. In each panel both the map view at 8 km depth and the vertical NS section (PQ in panel a) are shown. Stars represent the May 20 hypocenter projection (orange) and May 29 hypocenter location (yellow). In vertical sections, the dashed lines represent the CRUST1.0 discontinuities (Fig. 4). The Mirandola fault is assumed as a receiver fault.

In Fig. 11 we compare the ΔCFF on the Mirandola and Ferrara fault planes with the spatio-temporal distribution of seismicity. It is worth noting that almost all the seismicity tends to develop below the largest discontinuity in the elastic moduli at 3.3 km of depth. When we account for the slip occurred on the Mirandola fault in the T1 period (Fig. 11a), a negative CFF drop takes place within the area associated with this slip, while the surrounding area of the fault plane gets closer to failure, including the location of the May 29th hypocenter. If we don’t consider the slip that occurred on the Mirandola fault during T1 (Fig. 11b), the greatest CFF changes are confined within the eastern portion of the fault, near the Ferrara fault. However, we can note that the eastern part of the region of the

Mirandola fault, where aseismic slip occurred in T1, is loaded by slip occurred on the Ferrara fault only, in agreement with Cheloni et al. (2016) especially if we estimate ΔCFF as $\Delta\tau + \mu(\Delta\sigma_n - B\Delta\sigma_{kk}/3)$ (case of an isotropic pore pressurechange, see Fig. S11).

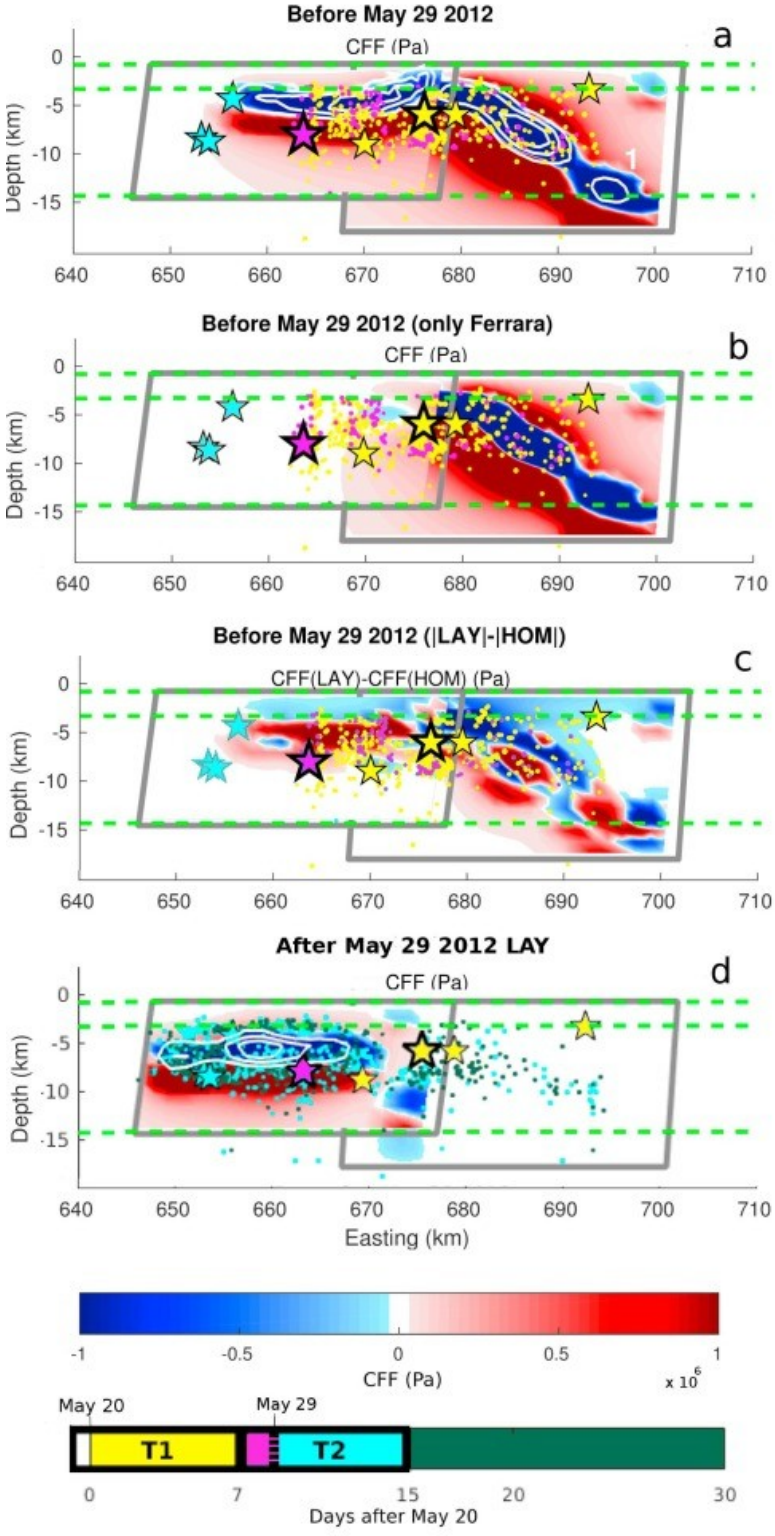

Fig. 11. View from the south of the seismicity distribution near the Ferrara and Mirandola faults before (panels a–c) and after (panel d) the May 29 mainshock. The event occurrence time is represented by the color scale (bottom right, black boxes delimit the T1 and T2 periods). Hypocenters are taken from Govoni et al. (2014), stars represent $M \geq 5$ events. For the T1 period and the LAY case, we also show the cumulative CFF change on the two faults planes with contours of slip values larger than 0.3 m on the Ferrara fault and larger than 0.1 m on the Mirandola fault (a) and the CFF contribution due to slip occurred on the Ferrara fault only (b), moreover panel (c) shows the difference between the absolute values of ΔCFF in the LAY case with respect to the HOM case. For the T2 period and the LAY case, panel (d) shows the cumulative CFF change on the two faults planes with contours of the maximum slip area. The green dashed lines represent the CRUST1.0 discontinuities (Fig. 4). Receiver fault mechanism is assumed to be the same as the one characterizing the fault plane where ΔCFF is evaluated.

Above 3.3 km of depth ΔCFF is positive in both HOM and LAY case (Fig. 10) while Fig. 11c shows that in the HOM case the near surface CFF increase is greater. Very few aftershocks develop above the strong discontinuity (Fig. 11c), where the HOM case overestimates the Coulomb stress increase. During T2 (Fig. 11d) there is a ΔCFF increase throughout the Mirandola fault plane, except for the area where coseismic slip occurred and we can note that most of the seismicity is focused around such area. In Fig. 11 all the events with $M_L \geq 5$ are placed in positive CFF zones, making it likely that the mechanical interaction between earthquakes played a very important role throughout the entire seismic sequence. Table S3 shows the ΔCFF computed in the LAY and HOM case for events with $M_L > 5$ for which the focal mechanisms are available (RCMT, http://rcmt2.bo.ingv.it, Pondrelli et al., 2002 and successive papers). In all the events the LAY case leads to a greater ΔCFF (up to 180% greater with respect to the HOM case), and we estimated positive ΔCFF in all events, except for the last one, occurred 4 days after the May 29th mainshock (M_L5.1, 06/03/2012). Moreover, Fig. 11 shows that seismicity lacks in correspondence with the relative maximum of slip or minimum of ΔCFF (zone #1 in Figs. 6c and 11a) at about 15 km of depth, perhaps suggesting an aseismic slip contribution.

6. Discussion and conclusions

In this work, we perform an inversion of the GPS and InSAR data, used by Pezzo et al. (2013), to obtain the slip distribution on the two fault planes associated with the May 20th and 29th mainshocks of the 2012 Emilia seismic sequence. Both fault planes are obtained from geological evidences and aftershocks distributions (Fig. 1). The latter were taken from Govoni et al. (2014). With respect to previous works we explored the influence of the rake angle and we implement an inversion method that accounts for an elastic medium with depth increasing rigidity and density. The InSAR displacement maps we use refer to two different time windows. The T1 period (from May 12 to May 27) cumulates deformation due to the first mainshock and the following 7 days of early post-seismic deformation of May 20th event. The T2 period (from May 27 to June 4) is representative of the coseismic and the first 6 days of early postseismic deformation of the May 29th event. Although the GPS data represent true coseismic displacements produced by the two mainshocks, our inversion results refer to the slip occurred in T1 and T2 periods since they are stable considering a 10%

magnitude increase of the GPS displacements vectors as representative of a possible postseismic deformation (Fig. S12). Within the T1 period, InSAR data suggest that both the Ferrara and Mirandola faults were active, in particular some slip, likely aseismic, occurred along the Mirandola fault plane (e.g. Pezzo et al., 2013). As in Pezzo et al. (2013) we perform an inversion of T1 data for the slip distribution on both the Ferrara and Mirandola faults, while T2 data are inverted for slip on the Mirandola fault only due to the limited area covered by the InSAR data used in the inversion. We also performed the inversion considering a third fault plane, as performed by Cheloni et al. (2016), but we found that the AICc value of the 3-faults model is larger than that of the 2-faults model, indicating that inserting a third fault does not lead to a modeling improvement with our dataset. For each period, we perform the inversion considering a homogeneous domain, HOM or a layered medium, LAY (see Fig. 4) based on CRUST1.0 crustal model. Performing inversions using the other two available crustal models, we find that the final slip distributions (Fig. S13) do not differ significantly (i.e. they are within 2σ errors) from the one obtained in the LAY case (Fig. 6), as all crustal models feature a main elastic discontinuity at about 3.3 km of depth. It is worth to notice that despite MAMBO and CRUST1.0 crustal models have different Vs, Vp and density profiles (especially above 3.3 km of depth, see Fig. S1), the inversion results we obtain using them are very similar because they have very similar Poisson's modulus and rigidity profiles, which are the parameters that affect the dislocation model.

We studied the influence of the rake angle on the Ferrara fault, finding that values larger than 80° are not supported by GPS data (Fig. 5). A suitable fit is obtained for rake values between 60° and 70°, and we choose the highest value because it is close to the one estimated by Cesca et al., 2013, Scognamiglio et al., 2016. Our choice implies a non-negligible east component of slip, still in agreement with the regional deformation field characterized by dominant about NE-SW shortening (Serpelloni et al., 2006, Devoti et al., 2011).

Comparing the results obtained in the HOM and LAY case, we can infer that the LAY case leads to a slight fit increase for the May 20 event, and a better fit for the May 29 event (RMS from 0.03 m, HOM, to 0.01 m, LAY, for the CSK2 map) and we also find that the maximum slip is larger in the HOM case within the range 10–15%. Similar results were obtained by Trasatti et al. (2011) for the L'Aquila earthquakein 2009 (Italy). If the rupture reaches the shallow layers, as in the case of the Ferrara fault, the slip obtained with the LAY case spreads more laterally (Fig. 6c), due to the smaller rigidity of the shallow layers. Indeed, for the LAY case, more slip is required near the surface to fit the same displacement, in agreement with Hearn and Burgmann (2005). If the rupture is deeper, as on the Mirandola fault during the T2 period, slip occurs at a greater depth for the LAY case (Fig. 6). We emphasize that only in the LAY case the hypocenter (Govoni et al., 2014) is located within the estimated rupture area: this suggests that in the HOM

case the bottom depth of the rupture can be underestimated, in agreement with Amoruso and Crescentini (2008). This result is stable with respect to the choice of the 1-D layered model employed (Fig. S13b). It is worth noting that the hypocenters of both mainshocks are placed at the edge of the correspondent slip zones (Fig. 6, Fig. 8), as it often occurs (Mai et al., 2005). When the Mirandola fault is allowed to slip during both T1 and T2 periods, our inversion results suggest about 10 km westward slip propagation passing from T1 to T2 (Fig. 8d), in agreement with the migration of seismicity observed during the sequence (Fig. 11). The equivalent seismic moment inferred from geodetic data in the T1 period overestimates the seismological value equivalent to $Mw = 6.1$ (RCMT) of about 5×10^{17} Nm which is the seismic moment equivalent to the inferred slip distribution on the Mirandola fault only. Accordingly, during the T1 period it is likely that the slip occurred on the Ferrara fault was mostly coseismic, while on the Mirandola fault it was mostly aseismic and possibly postseismic. However, on the Ferrara fault we find that a less resolved deep slip area, equivalent to a seismic moment of 3.9×10^{17} Nm, was not accompanied by relevant seismicity (area #1 in Fig. 11a), suggesting aseismic slip on it. A seismicity cut off can be identified around 15 km depth, although it seems to be shallower near the area #1 in Fig. 11a. The easternmost part of the Ferrara fault is known to have a high temperature gradient (Styles et al., 2014), suggesting a local rising of the brittle-ductile transition, thus the slip estimated in area #1 could possibly be related to transient aseismic processes occurring near the transition.

The ΔCFF computed from the slip distribution that occurred in the period T1 shows differences of about ±2 MPa in the near field, between the two cases, HOM and LAY (Fig. 10). For this latter, we observe a stress concentration just below the elastic discontinuity at 3.3 km depth (Fig. 11a), in agreement with literature results (Bonafede and Rivalta, 1999, Rybicki, 1971, Rybicki, 1973). Moreover, above the 3.3 km depth, the ΔCFF is overestimated up to 2 MPa in the HOM case. Since almost all the aftershocks occurred below this strong elastic discontinuity (Fig. 11) the assumption of a stratified model would possibly better explain the seismicity distribution compared to a homogeneous half-space, even if the lack of aftershocks there may be also due to the non-brittle rheology of the shallowest sediments layer. Since the stress variation in shallow layers strongly influences the effects of the earthquake on buildings, the use of a layered elastic model is required for a correct estimate of the seismic risk. At the May 29th event hypocenter, we obtain 0.35 MPa of positive CFF changes (~0.03 MPa larger in the LAY case than in the HOM case). We conclude that the second mainshock was most likely favored by the static stress transfer induced by the May 20th event. Unlike previous studies based on InSAR data, we still obtain a smaller but positive ΔCFF variation at the May 29th hypocenter location when neglecting the stress contribution of the aseismic slip on the Mirandola fault.

We can therefore conclude that the May 29th event was already facilitated by the May 20th mainshock and it was further (and mostly) favored by the aseismic slip that occurred on the Mirandola fault during the T1 period. Finally, we found that, with respect to the homogeneous half-space case, the layered model can lead to a deeper slip distribution and to an improvement in geodetic data modeling, lowering the RMS or M misfit. We also found that the LAY case leads to CFF changes that can be different from the ones obtained in the HOM case up to the order of MPa and it can emphasize the mechanical interaction of the seismic sequence according to the Coulomb failure theory.

Acknowledgements

We thank two anonymous referees for constructive comments and Prof. Paul Martin Mai for his useful suggestions on a preliminary version of this paper. The work by Antonio Pio Rinaldi was supported by a SNSF Ambizione Energy grant (PZENP2_160555). Letizia Anderlini was supported by MISE-DGRME project (cod. 0752.010). The whole data set is available upon request at massimo.nespoli2@unibo.it, giuseppe.pezzo@ingv.it.

References

Ader et al., 2012

T. Ader, *et al.* **Convergence rate across the Nepal Himalaya and interseismic coupling on the Main Himalayan Thrust: implications for seismic hazard**

J. Geophys. Res., 117 (2012), p. B04403, 10.1029/2011JB009071

Amoruso and Crescentini, 2008

A. Amoruso, L. Crescentini **Inversion of synthetic geodetic data for the 1997 Colfiorito events: clues on the effects of layering, assessment of model parameter PDFs, and model selection criteria**

Ann. Geophys. (2008), 10.4401/ag-3027

Anderlini et al., 2016

L. Anderlini, E. Serpelloni, M.E. Belardinelli **Creep and locking of a low-angle normal fault: insights from the Altotiberina fault in the Northern Apennines (Italy)**

Geophys. Res. Lett., 43 (2016), pp. 4321-4329, 10.1002/2016GL068604

Arnadottir and Segall, 1994

T. Arnadottir, P. Segall **The 1989 Loma Prieta earthquake imaged from inversion of geodetic data**

J. Geophys. Res., 99 (1994), pp. 21835-21855

Belardinelli et al., 2003

M.E. Belardinelli, L. Sandri, P. Baldi **The major event of the 1997 Umbria-Marche (Italy) sequence: what could we learn from DInSAR and GPS data?**

Geophys. J. Int., 153 (1) (2003), pp. 242-252, 10.1046/j.1365-246X.2003.01908.x

Biggs et al., 2006

J. Biggs, E. Bergman, B. Emmerson, G.J. Funning, J.Jackson, B. Parsons, T.J. Wright **Fault identification for buried strike-slip earthquakes using InSAR: the 1994 and 2004 Al Hoceima, Morocco earthquakes**

Geophys. J. Int., 166 (2006), pp. 1347-1362, 10.1111/j.1365-246X.2006.03071.x

Bigi et al., 1983

G. Bigi, G. Bonardi, R. Catalano, D. Cosentino, F.Lentini, M. Parotto, R. Sartori, P. Scandone, E. Turco (Eds.), Structural Model of Italy 1:500,000, CNR Progetto Finalizzato Geodinamica (1983)

Boccaletti and Martelli, 2004

M. Boccaletti, L. Martelli **Carta sismo-tettonica della Regione Emilia Romagna scala 1:250.000 e note illustrative**

SELCA, Firenze (2004)

Boccaletti et al., 2010

M. Boccaletti, G. Corti, L. Martelli **Recent and active tectonics of the external zone of the Northern Apennines (Italy)**

Int. J. Earth Sci. (2010), 10.1007/s00531-010-0545-y

Bonafede and Rivalta, 1999

M. Bonafede, E. Rivalta **On tensile cracks close to and across the interface between two welded elastic half-spaces**

Geophys. J. Int., 138 (1999), pp. 410-434, 10.1046/j.1365-246X.1999.00880.x

Bürgmann et al., 2005

R. Bürgmann, M.G. Kogan, G.M. Steblov, G.Hilley, E.V. Levin, E. Apel **Interseismic coupling and asperity distribution along the Kamchatka subduction zone**

J. Geophys. Res., 110 (2005), p. B07405, 10.1029/ 2005JB003648

Capaccioni et al., 2015

B. Capaccioni, F. Tassi, S. Cremonini, A. Sciarra, O. Vaselli **Ground heating and methane oxidation processes at shallow depth in Terre Calde di Medolla (Italy): observations and conceptual model**

J. Geophys. Res. Solid Earth, 120 (2015), pp. 3048-3064, 10.1002/2014JB011635

Cesca et al., 2013

S. Cesca, T. Braun, F. Maccaferri, L. Passarelli, E.Rivalta, T. Dahm **Source modelling of the M5–6 Emilia-Romagna, Italy, earthquakes (2012 May 20–29)**

Geophys. J. Int., 193 (2013), pp. 1658-1672, 10.1093/gji/ggt069

Cheloni et al., 2016

D. Cheloni, R. Giuliani, N. D'Agostino, M. Mattone, M. Bonano, G. Fornaro, R. L anari, D. Reale, S. Atzori **New insights into fault activation and stress transfer between en echelon thrusts: the 2012 Emilia, Northern Italy, earthquake sequence**

J. Geophys. Res. Solid Earth, 121 (2016), pp. 4742-4766, 10.1002/2016JB012823

Chiarabba et al., 2014

C. Chiarabba, P. De Gori, L. Improta, F.P.Lucente, M. Moretti, A. Govoni, M. Di Bona, L. Margheriti, A.Marchetti, A. Nardi **Frontal compression along the Apennines thrust system: the Emilia 2012 example from seismicity to crustal structure**

J. Geodyn., 82 (2014), pp. 98-109, 10.1016/j.jog.2014.09.003

Coleman and Li, 1996

T.F. Coleman, Y. Li **A reflective Newton method for minimizing a quadratic function subject to bounds on some of the variables**

SIAM J. Optim., 6 (4) (1996), pp. 1040-1058

Convertito et al., 2013

V. Convertito, F. Catalli, A. Emolo **Combining stress transfer and source directivity: the case of the 2012 Emilia seismic sequence**

Sci. Rep., 3 (2013), p. 3114, 10.1038/srep03114

Devoti et al., 2011

R. Devoti, A. Esposito, G. Pietrantonio, A.R. Pisani, F.Riguzzi **Evidence of large-scale deformation patterns from GPS data in the Italian subduction boundary**

Earth Planet. Sci. Lett., 311 (2011), pp. 1-12, 10.1016/j.epsl.2011. 09.034

Ganas et al., 2012

A. Ganas, Z. Roumelioti, K. Chousianitis **Static stress transfer from the May 20, 2012, M 6.1 Emilia-Romagna (northern Italy) earthquake using a co-seismic slip distribution model**

Ann. Geophys., 55 (4) (2012), pp. 655-662, 10.4401/ag-6176

Govoni et al., 2014

A. Govoni, A. Marchetti, P. De Gori, M. Di Bona, F.P.Lucente, L. Improta, D. Piccinini **The 2012 Emilia seismic sequence (Northern Italy): imaging the thrust fault system by accurate aftershock location**

Tectonophysics, 622 (2014), pp. 44-55, 10.1016/j.tecto.2014.02.013

Hardebeck et al., 1998

J. Hardebeck, J. Nazareth, E. Hauksson **The static stress change triggering model: constraints from two southern California aftershock sequences**

JGR, 103 (B10) (1998), pp. 24427-24437

Harris and Segall, 1987

R.A. Harris, P. Segall **Detection of a locked zone at depth on the Parkfield, California, segment of the San Andreas Fault**

J. Geophys. Res., 92 (B8) (1987), pp. 7945-7962, 10.1029/JB092iB08p07945

Harris, 1998

R.A. Harris **Introduction to special section: stress triggers, stress shadows, and implications for seismic hazard**

J. Geophys. Res., 103 (1998), pp. 24347-24358

Hearn and Burgmann, 2005

E.H. Hearn, R. Bürgmann **The effect of elastic layering on inversions of GPS data for coseismic slip and resulting stress changes: strike-slip earthquakes**

Bull. Seismol. Soc. Am., 95 (2005), pp. 1637-1653, 10.1785/0120040158

Hurvich and Tsai, 1989

C.M. Hurvich, C.L. Tsai **Regression and time series model selection in small samples**

Biometrika, 76 (2) (1989), pp. 297-307, 10.1093/biomet/76.2.297

Kilb et al., 2002

D. Kilb, J. Gomberg, P. Bodin **Aftershock triggering by complete Coulomb stress changes**

J. Geophys. Res., 107 (B4) (2002), 10.1029/2001JB000202

Laske et al., 2013

G. Laske, G. Masters, Z. Ma, M. Pasyanos **Update on CRUST1.0 – a 1-degree global model of earth’s crust**

Geophys. Res. Abstracts, 15 (2013)

Abstract EGU2013-2658

Lombardi and Bhattacharya, 2014

D. Lombardi, S. Bhattacharya **Liquefaction of soil in the Emilia-Romagna region after the 2012 Northern Italy earthquake sequence**

Nat. Hazards, 73 (3) (2014), pp. 1749-1770, 10.1007/s11069-014-1168-6

Mai et al., 2005

P.M. Mai, P. Spudich, J. Boatwright **Hypocenter locations in finite-source rupture models**

Bull. Seismol. Soc. Am., 95 (3) (2005), pp. 965-980

Marcaccio and Martinelli, 2012

M. Marcaccio, G. Martinelli **Effects on the groundwater levels of the May–June 2012 Emilia seismic sequence**

Ann. Geophys., 55 (2012), p. 4

Molinari et al., 2015

I. Molinari, A. Argnani, A. Morelli, P. Basini **Development and testing of a 3D seismic velocity model of the Po plain sedimentary basin, Italy**

Bull. Seismol. Soc. Am., 105 (2015), pp. 753-764

Nespoli et al., 2015

M. Nespoli, M. Todesco, B. Capaccioni, S. Cremonini **Ground heating and methane oxidation processes at shallow depth in Terre Calde di Medolla (Italy): numerical modeling**

J. Geophys. Res. Solid Earth, 120 (2015), pp. 3065-3076, 10.1002/2014JB011636

Nespoli et al., 2016

M. Nespoli, M. Todesco, E. Serpelloni, M.E.Belardinelli, M. Bonafede, M. Marcaccio, A.P. Rinaldi, L. Anderlini, A. Gualandi **Modeling earthquake effects on groundwater levels: evidences from the 2012 Emilia earthquake (Italy)**

Geofluids, 16 (3) (2016), pp. 452-463, 10.1111/gfl.12165

Okada, 1992

Y. Okada **Internal deformation due to shear and tensile faults in a half-space**

Bull. Seismol. Soc. Am., 82 (1992), pp. 1018-1040

Pondrelli et al., 2002

S. Pondrelli, A. Morelli, G. Ekström, S. Mazza, E.Boschi, A.M. Dziewonski **European-Mediterranean regional centroid-moment tensors: 1997–2000**

Phys. Earth Planet. Int., 130 (2002), pp. 71-101

Pedersen et al., 2003

R. Pedersen, S. Jónsson, T. Árnadóttir, F.Sigmundsson, K.L. Feigl **Fault slip distribution of two June 2000 6.5 earthquakes in South Iceland estimated from joint inversion of InSAR and GPS measurements**

Earth Planet. Sci. Lett., 213 (3) (2003), pp. 487-502, 10.1016/S0012-821X(03)00302-9

ISSN: 0012-821X

Pezzo et al., 2013

G. Pezzo, J.P.M. Boncori, C. Tolomei, S. Salvi, S.Atzori, A. Antonioli, E. Trasatti, F. Novali, E. Serpelloni, L.Candela, R. Giuliani **Coseismic deformation and source modeling of the May 2012 Emilia (Northern Italy)**

Seism. Res. Lett., 84 (2013), pp. 645-655

Picotti and Pazzaglia, 2008

V. Picotti, F.J. Pazzaglia **A new active tectonic model for the construction of the northern Apennines Mountain front near Bologna (Italy)**

J. Geophys. Res., 113 (2008), 10.1029/2007JB005307

Pizzi and Scisciani, 2012

A. Pizzi, V. Scisciani **The May 2012 Emilia (Italy) earthquakes: preliminary interpretations on the seismogenic source and the origin of the coseismic ground effects**

Ann. Geophys., 55 (4) (2012), pp. 751-757, 10.4401/ag-6171

Rajput et al., 2005

S. Rajput, V.K. Gahalaut, V.K. Sahu **Coulomb stress changes and aftershocks of recent Indian earthquakes**

Curr. Sci., 88 (6) (2005), pp. 576-588

Regione Emilia-Romagna and ENI-AGIP, 1998

Regione Emilia-Romagna, ENI-AGIP **Riserve idriche sotterranee della Regione Emilia Romagna**

S.EL.CA, Firenze (1998)

119 pp

Rybicki, 1971

K.R. Rybicki **The elastic residual field of a very long strike-slip fault in the presence of a discontinuity**

Bull. Seismol. Soc. Am., 61 (1971), pp. 79-92

Rybicki, 1973

K.R. Rybicki **Analysis of aftershocks on the basis of dislocation theory**

Phys. Earth Planet. Int., 7 (1973), pp. 409-422

Rovida et al., 2011

Rovida, A., Camassi, R., Gasperini, P., Stucchi, M., 2011. CPTI11, the 2011 Version of the Parametric Catalogue of Italian Earthquakes, Milano, Bologna. Available from: <http://emidius.mi.ingv.it/CPTI> (accessed November 2016).

Scognamiglio et al., 2012

L. Scognamiglio, L. Margheriti, F. Mele, E.Tinti, A. Bono, P. De Gori, V. Lauciani, F. Lucente, A. Mandiello, C. Marcocci, S. Mazza, S. Pintore, M. Quintiliani **The 2012 Pianura Padana Emiliana seismic sequence: locations, moment tensors and magnitudes**

Ann. Geophys., 55 (2012), pp. 549-559

Scognamiglio et al., 2016

L. Scognamiglio, F. Magnoni, E. Tinti, E.Casarotti **Uncertainty estimations for moment tensor inversions: the issue of the 2012 May 20 Emilia earthquake**

Geophys. J. Int., 206 (2) (2016), pp. 792-806, 10.1093/gji/ggw173

Serpelloni et al., 2006

E. Serpelloni, M. Anzidei, P. Baldi, G. Casula, A.Galvani **GPS measurement of active strains across the Apennines**

Ann. Geophys., 49 (1) (2006), pp. 319-329

Serpelloni et al., 2012

E. Serpelloni, L. Anderlini, A. Avallone, V.Cannelli, A. Cavaliere, D. Cheloni, C. D’Ambrosio, E.D’Anastasio, A. Esposito, G. Pietrantonio, A.R. Pisani, M.Anzidei , G. Cecere, N. D’Agostino, S. Del Mese, R. Devoti, A.Galvani, A. Massucci, D. Melini, F. Riguzzi, G. Selvaggi, V. Sepe **GPS observations of coseismic deformation following the May 20 and 29, 2012, Emilia seismic events (northern Italy): data, analysis and preliminary models**

Ann. Geophys., 55 (2012), p. 4

Styles et al., 2014

Styles, P., Gasparini, P., Huenges, E., Scandone, P., Lasocki, S., Terlizzese F., 2014. Report on the Hydrocarbon Exploration and Seismicity in Emilia Region

(ICHESE Report), 213. Available from: <http://mappegis.regione.emilia-romagna.it/gstatico/documenti/ICHESE/ICHESE_Report.pdf> (accessed 01.01.16).

Toscani et al., 2009

G. Toscani, P. Burrato, D. Di Bucci, S. Seno, G.Valensise **Plio-quaternary tectonic evolution of the northern Apennines thrust fronts (Bologna-Ferrara section, Italy): seismotectonic implications**

B. Soc. Geol. Ital., 128 (2009), pp. 605-613, 10.3301/IJG.2009.128.2.605

Trasatti et al., 2011

E. Trasatti, C. Kyriakopoulos, M. Chini **Finite element inversion of DInSAR data from the Mw 6.3 L'Aquila earthquake, 2009 (Italy)**

Geophys. Res. Lett., 38 (8) (2011), pp. 1-6, 10.1029/2011GL046714

Volpe and Piersanti, 2016

M. Volpe, A. Piersanti

Model. Earth Syst. Environ., 2 (2016), p. 32, 10.1007/s40808-016-0087-9

Wang et al., 2003

R. Wang, F.L. Martín, F. Roth **Computation of deformation induced by earthquakes in a multi-layered elastic crust – FORTRAN programs EDGRN/EDCMP**

Comput. Geosci., 29 (2) (2003), pp. 195-207

ISSN: 0098-3004

Zebker et al., 1994

H.A. Zebker, P.A. Rosen, R.M. Goldstein, A. Gabriel, C.L. Werner **On the derivation of coseismic displacement fields using differential radar interferometry: the Landers earthquake**

J. Geophys. Res., 99 (B10) (1994), pp. 19617-19634, 10.1029/94JB01179